King Saud University

Arabian Journal of Chemistry

www.ksu.edu.sa
www.sciencedirect.com

ORIGINAL ARTICLE

Highly efficient adsorption and removal of Chrysoidine Y from aqueous solution by magnetic graphene oxide nanocomposite

Yongmei Hao [a,*], Zhe Wang [a], Jiajia Gou [a], Suying Dong [b]

[a] College of Chemistry and Chemical Engineering, University of Chinese Academy of Sciences, 19(A) Yu Quan Road, Beijing 100049, China
[b] Beijing National Day School, No. 66 Yuquan Road, Haidian District, Beijing 100039, China

Abstract A new kind of adsorbent graphene oxide nanocomposite ($GO–Fe_3O_4$) for removal of Chrysoidine Y was synthesized using the modified Hummers method and co-precipitation. The synthesized $GO–Fe_3O_4$ was used as an adsorbent for the removal of Chrysoidine Y from aqueous solution. The effect of initial pH on the adsorption of Chrysoidine Y onto $GO–Fe_3O_4$ has been investigated. The adsorption kinetics, isotherm and thermodynamics also have been evaluated. The adsorption was strongly dependent on the pH of medium. The studies on the adsorption revealed that the adsorption process obeyed the Pseudo-second order kinetics model, and the rate-limiting step might be chemical sorption. And the Langmuir isotherm was applicable to describe the adsorption process. This hybrid showed a good performance for the removal of Chrysoidine Y from aqueous solution with an adsorption capacity of $344.83\ mg\ g^{-1}$ at room temperature, and could be easily removed from solution using a hand-held magnet in 10 min. Moreover, the adsorption mechanism was discussed and thermodynamic parameters were determined. Thermodynamic parameters indicated that the adsorption process was exothermic and spontaneous. Above all, the removal efficiency of $GO–Fe_3O_4$ was still kept at 96.0% when the concentration of dye was $100\ mg\ L^{-1}$ in polluted river. This work shows that $GO–Fe_3O_4$ is a suitable and efficient adsorbent in the removal of Chrysoidine Y from aqueous solution.

* Corresponding author. Tel.: +86 10 88256414; fax: +86 10 88256093.
E-mail address: ymhao@ucas.ac.cn (Y. Hao).
Peer review under responsibility of King Saud University.

Production and hosting by Elsevier
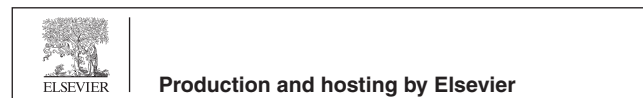
1. Introduction

Owing to growing population and rapid industrialization, the environmental problems get more and more attention. Areas near various industries, such as textile, paper making, metallurgy, carpet making, leather, distillery, and printing are polluted continuously because of the disposal of industrial

wastes. In particular, organic dye contamination is an issue of critical importance in environmental pollution. Organic dyes in environment are difficult to remove because most of them are nondegradable (Yan et al., 2011), and stable toward light due to their complex structures (Yan et al., 2011). Organic dye in environment can cause esthetic problems. But what is even worse is that organic dyes may cause chromosomal damage, high biotoxicity, potential mutagenic and carcinogenic effects on human beings (Ambashta and Sillanpaa, 2010).

Azo dyes, a class of dyes characterized by the presence of azo-group [—N=N—], are widely used in the textile, plastic, leather, rubber and food industries, and also synthesized in many industries (Mittal et al., 2010). Thus, the removal of dyes from wastewater is a challenging topic in environmental science and technology, and has attracted much attention in recent decades (Abdelkader et al., 2011). Many kinds of methods have been explored to remove the dyes from wastewater, such as photocatalytic degradation (Konstantinou and Albanis, 2004), flocculence (Rhymes and Smart, 2001), ion-exchange (Liu et al., 2007), extraction (Crini, 2005), membrane filtration (Lee et al., 2006), biological treatment (Kornaros and Lyberatos, 2006) and adsorption (Crini, 2006). On account of simplicity, ease of operation and high efficiency, adsorption is deemed as a high-efficient and economical technology (Crini, 2006). Adsorption combined with magnetic separation technology has gained much attention in recent years due to its easy phase separation from aqueous solutions and its capability of treating a mass of wastewater in few minutes (Luo and Zhang, 2009).

Graphene is one or several atomic layers of graphite, which possesses a special two-dimensional (2D) structure and low density, superior mechanical strength and high heat conductance (Service, 2009). It will be a good choice as an adsorbent for adsorbing various organic molecules due to its reactive and large specific surface. What is more, owing to its large delocalized π-electron system, graphene can form strong π-stacking interaction with benzene ring. So it is more suitable for adsorption of aromatic compounds (Allen et al., 2010) than other materials. Graphene oxide (GO) can be considered as oxidized graphene, which is exfoliated by strong oxidants, and it consists of a hexagonal network of covalently linked carbon atoms attached with oxygen-containing functional groups, such as epoxy, carboxyl and hydroxyl groups at various sites (Wu et al., 2011). Loading Fe_3O_4 nanoparticles onto graphene oxide could combine the relatively high adsorption capacity of graphene oxide and the separation convenience of magnetic materials. It has demonstrated that graphene-based materials can combine with cationic dyes through the π–π stacking interaction and van der Waals forces (Liu et al., 2012; Meral and Metin, 2014). However, as the adsorbents, graphene-based materials suffer from many defects, such as expensive processes and insufficient adsorption capacity (He et al., 2010; Wang et al., 2011; Zhou et al., 2014). Therefore, it is necessary to enhance the adsorption capacity of graphene-based materials using a simple and low cost method.

From the previous syntheses of magnetic graphene oxide nanocomposite (He et al., 2010; Xie et al., 2012; Yang et al., 2009), it could be known that these preparations were complicated. Even, one of these methods needed N_2 and one of them took a long time. Moreover, $GO–Fe_3O_4$ prepared in these methods had a low adsorption capacity for the removal of organic dyes (He et al., 2010; Xie et al., 2012).

Herein, we synthesized graphene oxide (GO) and magnetic graphene oxide nanocomposite ($GO–Fe_3O_4$) in a simple method and simultaneously increased adsorption capacity of $GO–Fe_3O_4$ as efficient as possible. Then the prepared $GO–Fe_3O_4$ was used to remove Chrysoidine Y from aqueous solutions. The effect of initial pH on adsorption, and the kinetics and adsorption isotherm of Chrysoidine Y adsorption onto the $GO–Fe_3O_4$ also have been investigated. This work may promote the preparation of magnetic graphene derivatives and facilitate the development of magnetic graphene-based materials.

2. Materials and methods

2.1. Materials

Graphite powder, Chrysoidine Y (CY, Fig. 1) and Iron (III) chloride hexahydrate were purchased from Sinopharm Chemical Reagent Co., Ltd. $NaNO_3$, $KMnO_4$, H_2SO_4 (wt: 95.0–98.0), HCl (wt: 36.0–8.0), $NH_3·H_2O$ (wt: 25) and H_2O_2 (wt: 30) solutions were purchased from Beijing Chemical Works. $FeCl_2·4H_2O$ was purchased from Shantou Xilong Chemical Factory of Guangdong. The deionized water was produced using a ULUPURE water purifier system with a resistivity of 18.25 MΩ. Besides graphite powder was of spectroscopically pure reagent, and all other chemicals were of analytical grade. All chemicals were used without further purification.

2.2. Synthesis of graphene oxide (GO)

Graphene oxide (GO) was synthesized using the modified Hummers method through oxidation of graphite powder (Chen et al., 2009; Madadrang et al., 2012). Typically, 1 g graphite powder and 0.5 g $NaNO_3$ were added into a 500 mL flask. Then, 46 mL of H_2SO_4 was added in the flask with stirring and simultaneously cooled by immersion in an ice bath at 0 °C. After vigorous stirring for 0.5 h, 6 g (37.97 mmol) $KMnO_4$ was slowly added into the flask and the temperature was kept below 20 °C. After that, the ice bath was removed and the mixture was constantly stirred at 35 °C for 2 h, and diluted with 92 mL deionized water under vigorously stirring with the temperature kept at 98 °C. Then 280 mL deionized water and 5 mL H_2O_2 solution were slowly added into the mixture, and the color of the mixture changed into bright yellow. The mixture was filtered and washed with 10% HCl solution for several times, and rinsed with deionized water for several times until the solution was neutral. The powder was dried at room temperature under vacuum. In this study, the amount of H_2SO_4 and $KMnO_4$ was increased and that of H_2O_2 decreased. From our previous report (Chen et al., 2013), it has been proved that the GO prepared in this simple method has a much higher adsorption capability.
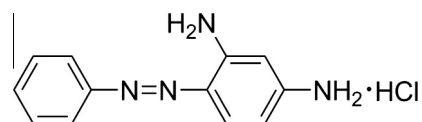

Figure 1   The structure of CY.

2.3. Synthesis of magnetic graphene oxide nanocomposite (GO–Fe₃O₄)

The magnetic graphene oxide nanocomposite (GO–Fe₃O₄) was in situ synthesized by chemical co-precipitation of Fe^{2+} and Fe^{3+} in alkaline solution in the presence of GO. The molar ratio of Fe^{2+}:Fe^{3+} was 1:2. To prepare GO–Fe₃O₄, 0.25 g GO was dispersed in 30 mL deionized water. The mixture was ultrasonicated (150 W, 40 kHz) for 50 min to form a homogeneous suspension, and this suspension was transferred into a 100 mL three-neck flask. The 10 mL aqueous solution dissolved with 0.40 g FeCl₃·6H₂O (1.48 mmol) and 0.15 g FeCl₂·4H₂O (0.75 mmol) was injected into the GO suspension. Afterward, 15 mL ammonia solution was added dropwise to precipitate the iron oxides under constant mechanical stirring for 1 h. The mixture was filtered and washed with 1:10 HCl solution several times, then rinsed with deionized water several times until the solution was neutral. Finally, the magnetic nanocomposite was dried at room temperature under vacuum (Wu et al., 2010).

2.4. Apparatus

X-ray diffraction (XRD) measurements were carried out on a MSAL-XD2 X-ray diffractometer, using a Cu Kα radiation (λ = 0.1541 nm) in the range of 5–80° (2θ) at 36 kV and 20 mA. The size and morphology of graphene oxide (GO) and magnetic graphene oxide nanocomposites (GO–Fe₃O₄) were observed by transmission electron microscopy (TEM) using H-7500 microscope (Hitachi, Japan). The Fourier transform infrared (FTIR) spectra of graphite powder (C), GO and GO–Fe₃O₄ were analyzed on a FTIR spectrometer (Thermo Nicolet 360-FTIR). The thermogravimetric analysis (TGA) was conducted on a thermal analyzer (SDT-Q600) under nitrogen atmosphere at a heating rate of 10 °C min⁻¹. The magnetic property was analyzed using a vibrating sample magnetometer (Lake Shore 7410 VSM) at room temperature. The UV-2550 UV–visible spectrophotometer (SHIMADZU, Japan) was used to record the absorption spectrum of samples and detect the concentration of Chrysoidine Y aqueous solution. The specific surface areas of samples were measured by N_2 adsorption-desorption isotherms at liquid nitrogen temperature using a Micromeritics Gemini V instrument.

2.5. Adsorption and desorption experiment

The removal of organic dye from aqueous solutions by GO–Fe₃O₄ was carried out using the following experimental procedures: 5 mg GO–Fe₃O₄ was added into 5 mL solutions with CY concentrations in the range of 100–1000 mg L⁻¹. After reaching the equilibrium, GO–Fe₃O₄ was removed from the solution by magnetic separation using permanent magnet and the final concentration of dye in the solution was measured with a UV–vis spectrophotometer at 455 nm. The removal percentage (%) and the removed quantity q_e (mg L⁻¹) of dye by GO–Fe₃O₄ were calculated from the concentration difference between the initial concentration (C_0) and the final one (C_e):

$$\text{Removal percentage } (\%) = \frac{C_o - C_e}{C_o} \times 100\%$$

$$q_e = \frac{C_o - C_e}{m} V$$

where C_0 (mg L⁻¹) represented the initial dye concentration, C_e (mg L⁻¹) was the final concentration of dye in the solution, V (L) was the volume of solution, and m (g) was the weight of GO–Fe₃O₄.

Desorption of CY was performed by mixing 5 mg of CY-loaded GO–Fe₃O₄ into 10 mL of HCl solution (0.1 mol L⁻¹), and sonicating 1 min. Then, the GO–Fe₃O₄ was separated from the solution by a permanent magnet, washed with distilled water several times, and dried in vacuum at 45 °C for next adsorption-desorption.

3. Results and discussion

3.1. Characterization studies

3.1.1. Morphology of GO and GO–Fe₃O₄

To investigate the morphology, TEM images of GO and GO–Fe₃O₄ were taken. The typical morphology of graphene oxide is shown in Fig. 2. As can be seen, the sheet-like, corrugated morphology exists, indicating the characteristics of single-layer GO sheets. There are small magnetite nanoparticles with an average size of 10 nm, uniformly decorate the surface of GO sheets. These results prove effectively that Fe₃O₄ nanoparticles are successfully modified on the surface of GO sheets.

3.1.2. Crystal structure of GO and GO–Fe₃O₄

XRD measurement was employed to investigate the phase and crystalline structure of the synthesized samples. The XRD patterns of graphite powder (C), GO and GO–Fe₃O₄ are shown in Fig. 3. It is observed that the XRD pattern of graphite powder shows the peaks at 2θ values of 26° (0 0 2) and 54° (0 0 4), while that of GO has peaks at 2θ values of 11° (0 0 1) and 42° (1 0 0). The XRD pattern of GO–Fe₃O₄ displays six characteristic peaks of Fe₃O₄ at about 2θ = 30.1°, 35.5°, 43.1°, 53.4°, 57.0° and 62.6°, corresponding to magnetite's indices (2 2 0), (3 1 1), (4 0 0), (4 2 2), (5 1 1) and (4 4 0) respectively. These results suggest that graphite powder is successfully oxidized to GO, and Fe₃O₄ nanoparticles are successfully attached to the surface of GO sheets. Compared with GO, the peak intensity of GO–Fe₃O₄ at 2θ = 11° is obviously reduced, and the peak at 2θ = 42° totally disappears. It indicates that GO–Fe₃O₄ has been exfoliated largely, and more disordered stacking and less agglomerated graphene sheets consist in the nanocomposite (Wu et al., 2010).

3.1.3. Surface functional group of GO and GO–Fe₃O₄

To confirm the attachment of Fe₃O₄ nanoparticles on the GO nanosheet surface, FTIR spectra of GO and GO–Fe₃O₄ were examined and the results are shown in Fig. 4. The absorption peaks at around 1714 cm⁻¹, 1616 cm⁻¹, 1365 cm⁻¹, 1045 cm⁻¹, which are attributed to the stretching vibration of C=O, stretching C=C, bending vibration of C—OH, and stretching vibration of C—O, respectively, indicate that the surface of GO possessed some oxygen-containing functional groups (Saleh, 2011; Saleh et al., 2011), and the characteristic peak presented at 586 cm⁻¹ confirms the Fe—O vibration. Several characteristic peaks of GO and Fe₃O₄ can be observed,
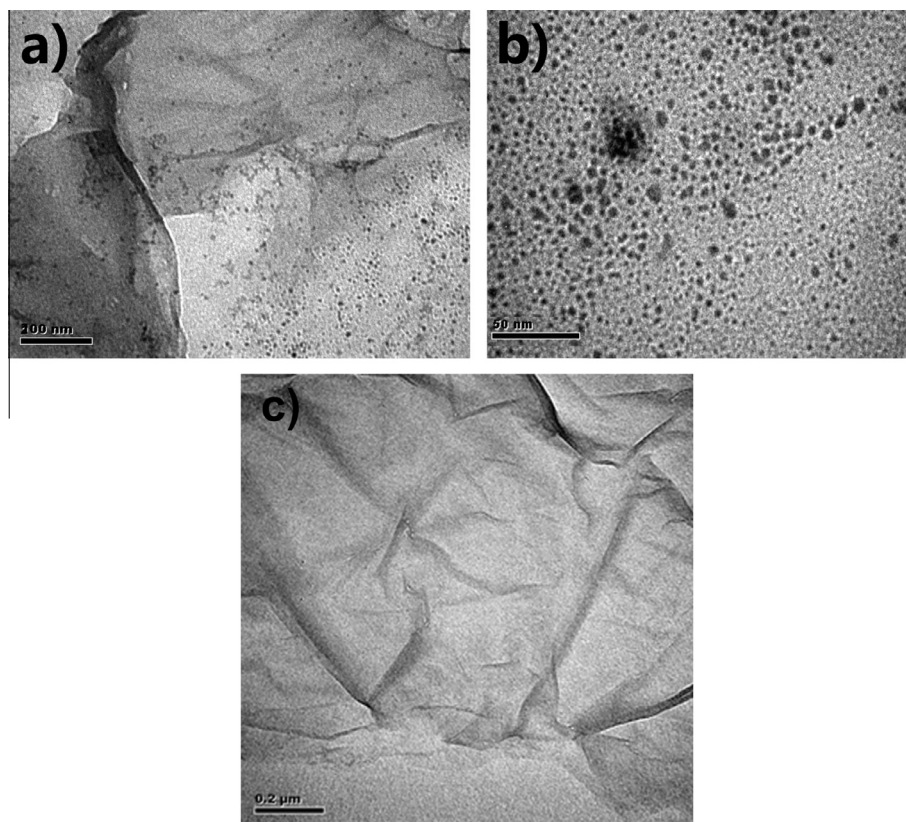
Figure 2   TEM images of GO–Fe$_3$O$_4$ (the resolution (a,c) ×200 nm, (b) ×50 nm) and GO (c).
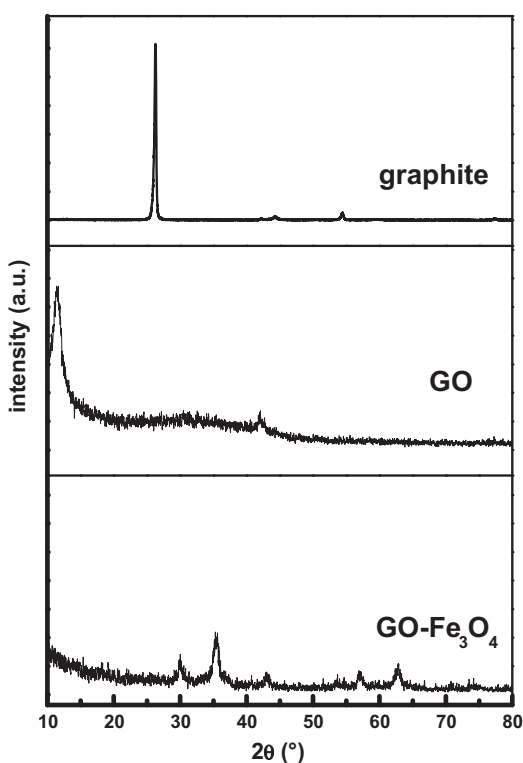

Figure 3   X-ray diffraction patterns of graphite powder (C), graphene oxide (GO) and magnetic graphene oxide nanocomposite (GO–Fe$_3$O$_4$).
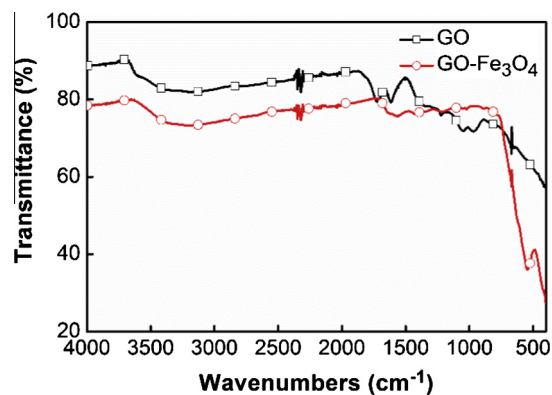
Figure 4   FTIR spectra of GO and GO–Fe$_3$O$_4$.

confirming the successful oxidation of graphite and Fe$_3$O$_4$ nanoparticles being successfully decorated on GO sheets, which is in accord with the results of XRD and TEM. It has been reported that the intensities of all the FTIR peaks of GO correlated to the oxygen containing groups decreased dramatically when GO was reduced (Dutta et al., 2013). Being similar with this previous results, the peak of GO at 1714 cm^{-1} decreases when GO is decorated with Fe$_3$O$_4$ nanoparticles in this study, which demonstrates that the GO is reduced partially by the adsorption of Fe$_3$O$_4$ nanoparticles on it. Furthermore, owing to the sorbent's abundant oxygen-containing groups such as epoxy, carboxyl and hydroxyl groups, the protonated Chrysoidine Y molecules could be

adsorbed onto GO–Fe$_3$O$_4$ through the anionic-cationic interaction.

3.1.4. Thermo-gravimetric analysis results

The content of oxygen-containing groups on the surface of GO and GO–Fe$_3$O$_4$, which determined the adsorption capacity of GO–Fe$_3$O$_4$, could be determined with the TGA technique via oxidative decomposition which was carried out in nitrogen atmosphere from room temperature to 800 °C at a rate of 10 °C min^{-1}. Fig. 5 shows the representative TGA curves of GO and GO–Fe$_3$O$_4$. As shown in Fig. 5, there are three weight loss processes. Firstly, a slight weight loss that occurred below 100 °C can be ascribed to the evaporation of adsorbed water molecules. Secondly, the marked weight loss occurs from 100 to 250 °C, which can be assigned to the removal of labile oxygen-containing functional groups such as epoxy, carboxyl and hydroxyl vapors from the sorbent. Finally, a slight weight loss appeared from 250 to 800 °C is caused by the decomposition of the carbon skeleton (Wang et al., 2010). Moreover, comparing the two curves, the weight losses of GO and GO–Fe$_3$O$_4$ at 100–250 °C are about 36.72% and 27.04%, respectively. These results indicate that both GO and GO–Fe$_3$O$_4$ have abundant oxygen-containing groups on their surfaces, and Fe$_3$O$_4$ nanoparticles have replaced some oxygen-containing groups.

3.1.5. Magnetic results

Fig. 6a shows a hysteresis loop measured at room temperature. As expected, the GO–Fe$_3$O$_4$ exhibits no remanence or coercivity at room temperature, revealing its superparamagnetic characteristics (Ge et al., 2008). Because of the microscale of Fe$_3$O$_4$ being modified on GO, the saturation magnetization of GO–Fe$_3$O$_4$ is 8 emu g^{-1}, but it is sufficient for magnetic separation by an ordinary magnet. Fig. 6b shows photograph of GO–Fe$_3$O$_4$ adsorption and the separation under an external magnetic field. The GO–Fe$_3$O$_4$ dispersed in aqueous solution can be easily collected by a handle magnet within 1–2 min and the aqueous solution becomes colorless, and GO–Fe$_3$O$_4$ can be readily re-dispersed with slight shake after removing the magnetic field. The results reveal the good magnetic separation characteristics of GO–Fe$_3$O$_4$, suggesting GO–Fe$_3$O$_4$ can be used as a magnetic adsorbent to remove some organic contaminants from aqueous solutions.

Figure 6a   Hysteresis loop of GO–Fe$_3$O$_4$ nanocomposite at room temperature.

Figure 6b   Photograph of CY solution (left), the solution after adsorption by GO–Fe$_3$O$_4$ and separation with a magnet (right).
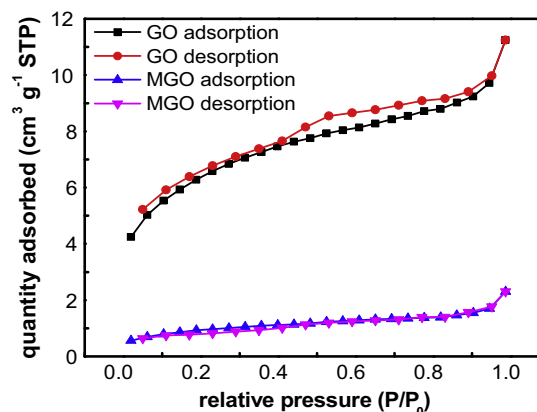
Figure 7   Nitrogen adsorption–desorption isotherms of GO and GO–Fe$_3$O$_4$.

3.1.6. Surface areas and absorption spectrum of GO and GO–Fe$_3$O$_4$

The specific surface areas of samples were measured by N$_2$ adsorption-desorption isotherms. Both GO and GO–Fe$_3$O$_4$ show typical "type IV" N$_2$ adsorption-desorption isotherms (Fig. 7), and the specific surface areas of GO and GO–Fe$_3$O$_4$ are 22.11 and 3.312 m^2 g^{-1}, respectively.

Figure 5   TGA diagram of GO and GO–Fe$_3$O$_4$.

Fig. 8 shows the absorption spectra of GO and GO–Fe$_3$O$_4$. GO displays a characteristic peak at 228 nm corresponding to $\pi \to \pi^*$ transitions of aromatic C—C bonds, while for GO–Fe$_3$O$_4$, the absorption peak blueshifts to 224 nm, indicating that Fe$_3$O$_4$ particles are covalently attached onto GO surface (Chen et al., 2013).

3.2. Adsorption of CY

3.2.1. Effect of initial pH on adsorption

Since acidity not only affects the solution chemistry of contaminants (i.e. hydrolysis, redox reaction, polymerization and coordination) but also has a strong influence on the ionic state of functional groups on the surface of adsorbent, and the initial pH of the solution is one of the most important parameters in the adsorption of environmental contaminants in aqueous solution. In this work, the adsorption quantity and removal percentage of CY by GO–Fe$_3$O$_4$ were detected with pH values ranging from 3 to 11. As presented in Fig. 9, the adsorption quantity of GO–Fe$_3$O$_4$ increases from 154.61 to 193.94 mg g^{-1} and removal percentage increases from 77.30% to 96.97% when the initial pH is varied from 3 to 6, and keeps constant over the pH range of 6–8. With the pH value increased from 8 to 11, the adsorption capacity and removal percentage decrease. Considering the pH values of water in nature, the experiments in this study were performed at pH 7.0.

3.2.2. Adsorption kinetics

The adsorption kinetics information has a significant practical value. Rapid reaction time could facilitate smaller reactor volumes and ensure efficiency and economy. The adsorption kinetics was determined to understand the adsorption property of GO–Fe$_3$O$_4$. Kinetics experiments were carried out by adding 5.0 mg of new prepared GO–Fe$_3$O$_4$ to 5.0 mL aqueous solution containing 200, 300 and 400 mg L^{-1} CY at room temperature. The effect of adsorption time on the removal of CY is shown in Fig. 10. The result displays that a fast adsorption process occurs during the first few minutes and then reaches equilibrium. It is observed that the adsorption equilibrium time is about 30 min for all the concentrations, which attributes to the adequate free adsorptive sites and a high
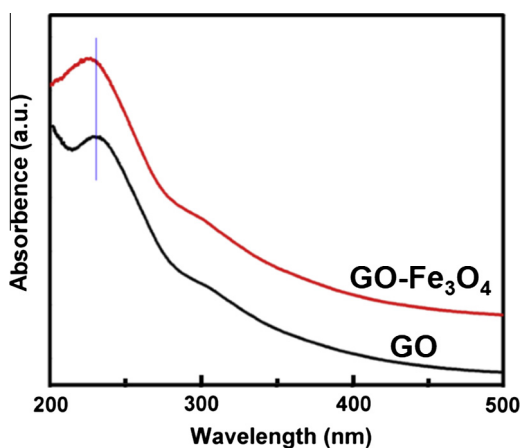
concentration gradient. This rapid adsorption indicates that the adsorption occurs mainly on the surface of adsorbent.

In order to understand the adsorption kinetics, four different kinetic models were used to fit the experimental data. They are the Pseudo-first-order (Ho and McKay, 1998), Pseudo-second-order (Ho and McKay, 1999), Intraparticle diffusion and Elovich models (Chien and Clayton, 1980; Hao et al., 2010). The Pseudo-first-order model rate equation is expressed as follows:

$$\ln(q_e - q_t) = \ln q_e - k_1 t$$

where q_e is the amount of dye adsorbed by adsorbent at equilibrium (mg g^{-1}), q_t is the amount of dye adsorbed at time t (mg g^{-1}), and k_1 is the rate constant (min^{-1}). By plotting $\ln(q_e - q_t)$ versus t, the k_1 and the calculated equilibrium sorption capacities $q_{e,cal}$ could be obtained from the slope and intercept of plots in Fig. 11(a), respectively.

The Pseudo-second-order model is given by the following equation (Chen et al., 2010):

$$\frac{t}{q_t} = \frac{1}{k_2 q_e^2} + \frac{t}{q_e}$$

where k_2 is the Pseudo-second-order model rate constant (g mg^{-1} min^{-1}) and q_e is the sorption capacity at equilibrium. k_2 and q_e can be determined respectively from the intercept and slope of the plot which is obtained by plotting t/q_t versus t (Fig. 11(b)).

The Intraparticle diffusion rate equation is provided as follows:

$$q_t = k_i t^{1/2} + C$$

where C is the constant related to the thickness of the boundary layer (mg g^{-1}), and k_i is the intraparticle diffusion rate constant (mg g^{-1} min$^{-1/2}$). The adsorption process is controlled only by intraparticle diffusion when the plot of q_t versus $t^{1/2}$ gives a straight line. However, if the data exhibit multi-linear plots, two or more parameters influence the adsorption process. Based on the equation, the values of q_t correlated linearly with values of $t^{1/2}$ and the rate constant k_i could be directly evaluated from the slope of the regression line (Fig. 11(c)) before reaching equilibrium. The beginning straight line represents macropore diffusion and the second one depicts micropore diffusion. Significantly, the C values obtained from the intercept in this work are not zero, indicating that intraparticle diffusion may not be the only controlling factor in determining the kinetics of the adsorption process (Hameed, 2008).

Elovich model rate equation is indicated as

$$q_t = \frac{1}{\beta} \ln(\alpha\beta) + \frac{1}{\beta} \ln$$

It is used to describe chemical adsorption on highly heterogeneous adsorbents, where α (g g^{-1} min^{-2}) and β (g mg^{-1} min^{-1}) are the equilibrium rate constants. These constants can be obtained from the slope and intercept of initial part of plot which is shown in Fig. 11(d) before reaching equilibrium.

From the parameters listed in Table 1, it suggests that the adsorption kinetics follows the Pseudo-second-order kinetic model much better than the other models because of its higher correlation coefficients (R^2), which also indicates that the adsorption is a fast process. Based on the Pseudo-second-order model (Vadivelan and Kumar, 2005), it can be
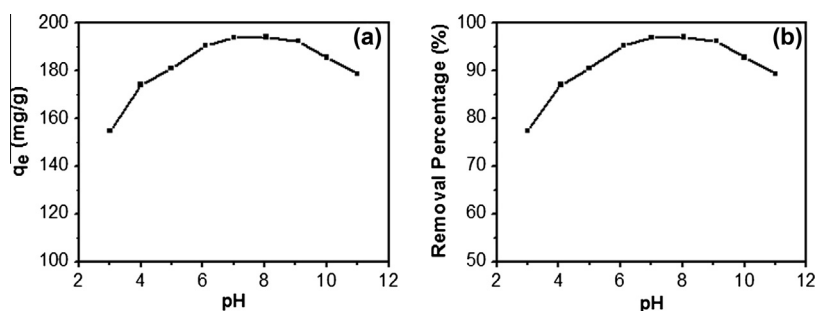

Figure 8   Absorption spectra of GO and GO–Fe$_3$O$_4$.

Figure 9 Effect of solution pH on the adsorption of CY by GO–Fe$_3$O$_4$ (initial CY concentration: 200 mg L^{-1}; contact time: 60 min).
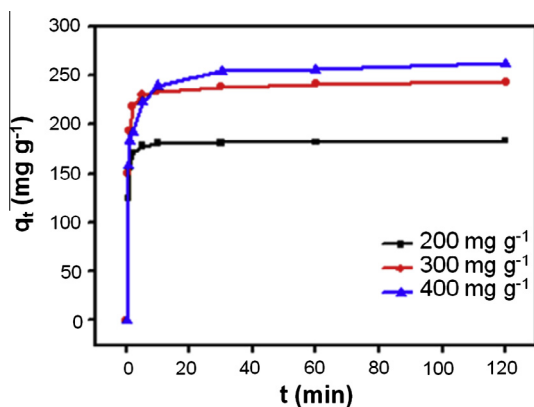

Figure 10 Effect of adsorption time on the adsorption capacity for CY onto GO–Fe$_3$O$_4$ nanocomposite at different initial CY concentration (200 mg L^{-1}, 300 mg L^{-1} and 400 mg L^{-1}) at room temperature; dosage of GO–Fe$_3$O$_4$: 5.0 mg.

concluded that the adsorption of CY onto GO–Fe$_3$O$_4$ is a chemical adsorption, and more than one step may be involved in the adsorption process.

3.2.3. Adsorption isotherms

To further understand the adsorption mechanism and quantitatively describe adsorption capacities, the adsorption data were analyzed by the Langmuir and Freundlich isotherm models (Allen et al., 2004).

The Langmuir isotherm assumes the monolayer coverage of adsorbate over a homogeneous adsorbent surface. It has found successful application in many monolayer adsorption processes. This isotherm is depicted by the following equation:

$$\frac{C_e}{q_e} = \frac{C_e}{q_m} + \frac{1}{K_L q_m}$$

where q_e and C_e are the adsorption quantity (mg g^{-1}) and concentration of the adsorbate at equilibrium (mg L^{-1}), while q_m and K_L represent adsorption capacity of adsorbent (mg g^{-1})
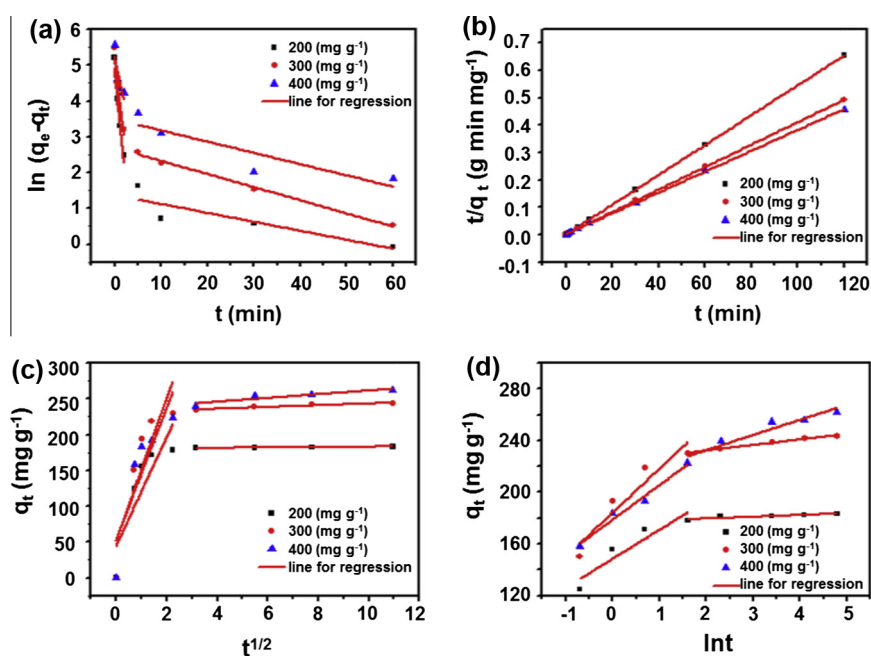

Figure 11 The fitting of different kinetic models for CY adsorption onto GO–Fe$_3$O$_4$ at different initial concentration (200 mg L^{-1}, 300 mg L^{-1} and 400 mg L^{-1}) at room temperature ((a) Pseudo-first-order, (b) Pseudo-second-order, (c) Intraparticle diffusion and (d) Elovich).

Table 1 Adsorption kinetic parameters for the adsorption of Chrysoidine Y onto GO–Fe$_3$O$_4$ nanocomposite at various concentrations.

Kinetic models and parameters	Concentration (mg L^{-1})		
	200	300	400
Pseudo-first-order			
k_1 (min^{-1})	1.3167	1.1	0.5946
$q_{e,cal}$ (mg g^{-1})	136.62	190.55	185.38
R^2	0.9084	0.9093	0.5672
Pseudo-second-order			
k_2 (g mg^{-1} min^{-1})	0.0326	0.0134	0.0058
q_e (mg g^{-1})	183.15	243.31	262.47
R^2	0.9999	0.9999	0.9998
Intraparticle diffusion			
k_i (mg g^{-1} min$^{-1/2}$)	75.88	99.39	92.33
C (mg g^{-1})	44.75	51.97	52.71
R^2	0.6507	0.7011	0.6831
Elovich			
α (g g^{-1} min^{-2})	16.923	7.668	21.689
β (g mg^{-1} min^{-1})	0.045	0.029	0.037
R^2	0.8108	0.8462	0.9661

Table 3 Comparison of the adsorption capacities of various adsorbents for CY.

Adsorbents	Adsorption capacity (mg g^{-1})	Contact time (min)	Ref.
Bottom ash	18.08	180	Mittal et al. (2010)
De-oiled soy	8.33	180	Mittal et al. (2010)
FC	57.3	180	Nurchi et al. (2014)
GC	44.6	180	Nurchi et al. (2014)
Beads	61.5	180	Nurchi et al. (2014)
GO	680.3	30	This work
Fe$_3$O$_4$	63.94	30	This work
GO–Fe$_3$O$_4$	359.71	30	This work

and the Langmuir adsorption equilibrium constant (L mg^{-1}). The results are shown in Table 2, and the adsorption capacities (q_m) of GO–Fe$_3$O$_4$ at 20 °C and 50 °C are 344.83 and 285.71 mg g^{-1}, respectively. Compared with some previous adsorbents (Table 3), the adsorption capacity of GO–Fe$_3$O$_4$ is much higher, indicating that GO–Fe$_3$O$_4$ is an ideal adsorbent for the removal of CY from aqueous solution. Moreover, it is noticed that the adsorption capacity decreases when the temperature increases from 20 °C to 50 °C, suggesting that this adsorption is exothermic.

The type of Langmuir isotherm can be used to predict whether the adsorption is favorable or unfavorable in terms of either the equilibrium parameter or a dimensionless constant separation factor R_L, which is defined by the following equation:

$$R_L = \frac{1}{1 + K_L C_o}$$

Here C_o (mg L^{-1}) is the initial concentration of adsorbate. The R_L indicates the type of isotherm to be irreversible ($R_L = 0$), favorable ($0 < R_L < 1$), linear ($R_L = 1$) or unfavorable

($R_L > 1$). The R_L values in this work are in the range of 0.024–0.31, which indicates a favorable adsorption between CY and GO–Fe$_3$O$_4$.

The Freundlich model is applied to monolayer adsorption but not a saturation-type isotherm. It is an empirical equation assuming that the adsorption process takes place on heterogeneous surfaces. The Freundlich adsorption equation is given as follows (Luo and Zhang, 2009):

$$\ln q_e = \frac{1}{n} \ln C_e + \ln K_F$$

where K_F (mg g^{-1}) is the Freundlich constant indicating adsorption capacity, and n is an empirical parameter related to the intensity of adsorption. The value of n varies with the heterogeneity of the adsorbent and for favorable adsorption process the value of n should lie in the range of 1–10. It is illustrated that the value of n in the range 2–10 represents good, 1–2 moderately difficult, and less than 1 poor adsorption (Hao et al., 2010). From Table 2, the values of n at 20 and 50 °C are 4.8685 and 4.7939, showing a good adsorption. Moreover, the R^2 values at 20 °C for the Langmuir and Freundlich models in Table 2 are 0.9971 and 0.9662, which demonstrates that the Langmuir model fits the adsorption data better than the Freundlich one, and states that the adsorption of CY onto GO–Fe$_3$O$_4$ may be a monolayer coverage process.

3.2.4. Thermodynamic parameters

Considering the practical application, thermodynamic parameters should be detected in order to determine which process will take place spontaneously. Thermodynamic parameters including Gibbs free energy ($\triangle G^0$), enthalpy change ($\triangle H^0$) and change in entropy ($\triangle S^0$) are obtained according to the following formulas:

$$\Delta G^0 = -RT \ln K_L$$

$$\Delta G^0 = \Delta H^0 - T\Delta S^0$$

Here R is the gas constant, T is the absolute temperature, and K_L (q_e/C_e) is Langmuir constant at various temperatures when the concentration terms are expressed in L/mol. The values of $\triangle H^0$ and $\triangle S^0$ were calculated from the intercept and slop of the plot of $\triangle G^0$ vs. T. All these thermodynamic parameters are listed in Table 4.

Table 2 Adsorption isotherm parameters for the adsorption of CY onto GO–Fe$_3$O$_4$ at different temperatures at various concentrations.

Isotherms	Parameters	Temperature	
		20 °C	50 °C
Langmuir	q_m (mg g^{-1})	344.83	285.71
	K_L (L mg^{-1})	0.040	0.022
	R_L range	0.024–0.20	0.043–0.31
	R^2	0.9971	0.9959
Freundlich	K_F (mg g^{-1})	93.9347	71.3003
	n	4.8685	4.7939
	R^2	0.9662	0.9939

Table 4 Thermodynamic parameters of CY adsorption onto GO–Fe_3O_4 at different temperatures.

| T (K)	ΔG^0 (kJ/mol)	ΔH^0 (kJ/mol)	ΔS^0 (J/mol K)
293	−2.399	−8.192	−19.77
313	−2.004		
323	−1.806		

The negative values of $\triangle G^0$ at different temperatures indicate spontaneity and feasibility of the adsorption process. Moreover, the values of $\triangle G^0$ in Table 4 are less than 10 kJ/mol, which suggest that the adsorption process is physisorption (Li et al., 2014). From the minus value of $\triangle H^0$, it further reveals that the adsorption reaction is exothermic and the adsorption process is energetically stable, which is also supported by the decrease in the mass of adsorbed CY with the increase in temperature. The negative value of $\triangle S^0$ confirms the decreasing randomness at the solid-solution interface during the adsorption of CY onto GO–Fe_3O_4. These results are in accordance with these previous results (Dong et al., 2014; Li et al., 2014; Shi et al., 2014).

3.3. Adsorption mechanism

Based on the experimental results of initial pH on adsorption, adsorption mechanism can be analyzed. At pH lower than 5.4, the positively charged (protonated) species (CYH^+) is the prevalent form of CY (Nurchi et al., 2014), while the carboxyl groups on the GO sheets are prone to be protonated. Therefore, the adsorption efficiency for cationic dye CYH^+ is quite low in acidic media. With pH changes from 6 to 3, the removal percentage decreases due to more and more protonated carboxyl groups on the GO–Fe_3O_4. At higher pH values (8–11), there are plenty of OH^{-1} ions in the aqueous solutions, and the amino groups of CY are prone to combine with OH^{-1}, leading to a decreased amount of CY adsorbed onto GO–Fe_3O_4. These results indicate the anion-cation interaction between GO–Fe_3O_4 and the dye molecules.

At pH varies from 6 to 8, the neutral species of CY (Nurchi et al., 2014) is predominant. Thus, the highest removal capacity of GO–Fe_3O_4 in the pH range of 6–8 may come from π–π stacking interaction between benzene rings of CY and large delocalized π-electron system of GO in GO–Fe_3O_4 structure (Chen et al., 2013). Furthermore, the comparison of adsorption capacity among Fe_3O_4, GO and GO–Fe_3O_4 in Table 3 also implies that GO should be contributed to the high capacity of GO–Fe_3O_4.

From the above analysis, the adsorption between CY and GO–Fe_3O_4 include anion-cation interaction and π–π stacking
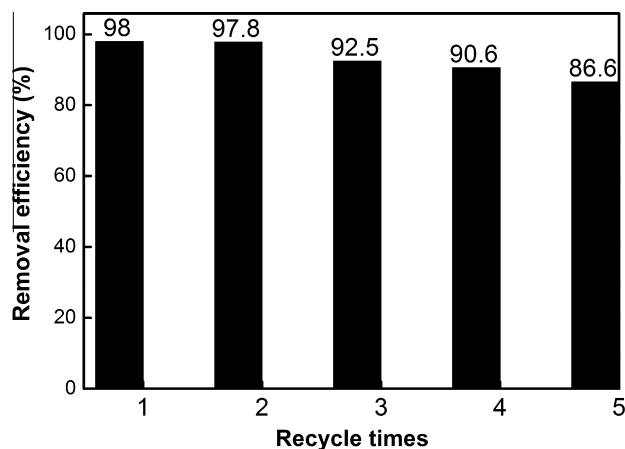
Figure 12 Reusability study of GO–Fe_3O_4.

interaction. This is in accordance with thermodynamics study which suggests that the adsorption process is physisorption.

3.4. Influence of real water matrix

With a view to evaluate the effects of matrix on removal efficiency, the samples of polluted river water spiked with three different concentrations of CY were used. As listed in Table 5, the results reveal that the removal efficiency of CY is still kept at 95.98% in a real water sample when the concentration of dye is 100 mg L^{-1}. There is no significant influence of water matrix on the removal of CY. These results indicate that GO–Fe_3O_4 has a great potential in practical application in the removal of CY from wastewater.

3.5. Reusability of GO–Fe_3O_4 for CY removal

Taking into account the practical application, the adsorption–desorption cycle was repeated 5 times. In the analysis of the influence of pH on the removal, it was expected that acid would be an effective agent for desorption. The experiment results indicate that CY could be desorbed completely by 1 min sonication in the presence of 0.1 mol L^{-1} HCl.

As shown in Fig. 12, although the adsorption capacity of GO–Fe_3O_4 decreases a little for each successive run, the removal efficiency of GO–Fe_3O_4 still remains at 86.6% after 5 adsorption–desorption cycles. Since 0.1 mol L^{-1} HCl solution is used as the desorbing agent and the adsorbent is dried in an oven during regeneration, each adsorption-desorption process must undergo an acid-treated and heat-treated process. Thus, the reusability of GO–Fe_3O_4 as shown in Fig. 12 also indicates its good stability.

Table 5 The pH, concentration of COD and other metal ions in water and comparison of removal efficiency of GO–Fe_3O_4 nanocomposite for Chrysoidine Y from de-ionized water and polluted river water.

Matrix	pH	COD (mg L^{-1})	Fe (ug L^{-1})	Ca (mg L^{-1})	Mg (mg L^{-1})	50[a]	100[a]	200[a]
De-ionized water	6.8	0	0	0	0	100[b]	97.9[b]	91.6[b]
River	6.1	30	50.2	88.1	10.9	100[b]	96.0[b]	90.9[b]

[a] Initial concentration (mg L^{-1}) measured after spiked with 50, 100 and 200 mg L^{-1} Chrysoidine Y.
[b] Removal efficiency of GO–Fe_3O_4 for Chrysoidine Y (%) from de-ionized water and polluted river water.

4. Conclusion

GO–Fe$_3$O$_4$ was synthesized by a simple and low-cost method. XRD, TEM, FTIR, TGA and VSM were employed to characterize its morphology, structure and magnetic property and so on. The synthesized GO–Fe$_3$O$_4$ was used as an adsorbent to remove Chrysoidine Y from an aqueous solution. The adsorption was strongly dependent on pH, was very rapid and could reach adsorption equilibrium within 30 min. The results showed that the adsorption kinetics and isotherm obeyed the Pseudo-second-order and Langmuir isotherm models, respectively. The adsorption capacity was 344.83 mg g^{-1} at room temperature, and π–π stacking interaction was attributed to this high adsorption capacity. GO–Fe$_3$O$_4$ could easily be separated from an aqueous solution with magnetic separation in a short time. There was no significant influence of water matrix on the removal of cationic dye Chrysoidine Y. These results indicate that the GO–Fe$_3$O$_4$ can be used as a suitable and efficient adsorbent in the removal of Chrysoidine Y from wastewater.

Acknowledgment

References

Abdelkader, N.B.H., Bentouami, A., Derriche, Z., Bettahar, N., de Menorval, L.C., 2011. Synthesis and characterization of Mg–Fe layer double hydroxides and its application on adsorption of Orange G from aqueous solution. Chem. Eng. J. 169 (1–3), 231–238.

Allen, M.J., Tung, V.C., Kaner, R.B., 2010. Honeycomb carbon: a review of graphene. Chem. Rev. 110 (1), 132–145.

Allen, S.J., McKay, G., Porter, J.F., 2004. Adsorption isotherm models for basic dye adsorption by peat in single and binary component systems. J. Colloid Interface Sci. 280 (2), 322–333.

Ambashta, R.D., Sillanpaa, M., 2010. Water purification using magnetic assistance. A review. J. Hazard. Mater. 180 (1–3), 38–49.

Chen, C., Yang, Q.H., Yang, Y., Lv, W., Wen, Y., Hou, P.X., Wang, M., Cheng, H.M., 2009. Self-assembled free-standing graphite oxide membrane. Adv. Mater. 21 (29), 3007–3011.

Chen, J.Y., Hao, Y.M., Liu, Y., Gou, J.J., 2013. Magnetic graphene oxides as highly effective adsorbents for rapid removal of a cationic dye rhodamine B from aqueous solutions. RSC Adv. 3, 7254–7258.

Chen, S., Zhang, J., Zhang, C., Yue, Q., Li, Y., Li, C., 2010. Equilibrium and kinetic studies of methyl orange and methyl violet adsorption on activated carbon derived from Phragmites australis. Desalination 252 (1–3), 149–156.

Chien, S.H., Clayton, W.R., 1980. Application of Elovich equation to the kinetics of phosphate release and sorption in soils. Soil Sci. Soc. Am. J. 44 (2), 265–268.

Crini, G., 2005. Recent developments in polysaccharide-based materials used as adsorbents in wastewater treatment. Prog. Polym. Sci. 30 (1), 38–70.

Crini, G., 2006. Non-conventional low-cost adsorbents for dye removal: a review. Bioresource Technol. 97 (9), 1061–1085.

Dong, Z.H., Wang, D., Liu, X., Pei, X.F., Chen, L.W., Jin, J., 2014. Bio-inspired surface-functionalization of graphene oxide for the adsorption of organic dyes and heavy metal ions with a superhigh capacity. J. Mater. Chem. A 2, 5034–5040.

Dutta, S., Sarkar, S., Ray, C., Pal, T., 2013. Benzoin derived reduced graphene oxide (rGO) and its nanocomposite: application in dye removal and peroxidase-like activity. RSC Adv. 3, 21475–21483.

Ge, J., Zhang, Q., Zhang, T., Yin, Y., 2008. Core-satellite nanocomposite catalysts protected by a porous silica shell: controllable reactivity, high stability, and magnetic recyclability. Angew. Chem. Int. Ed. 47 (46), 8924–8928.

Hameed, B.H., 2008. Equilibrium and kinetic studies of methyl violet sorption by agricultural waste. J. Hazard. Mater. 154 (1–3), 204–212.

Hao, Y.M., Chen, M., Hu, Z.B., 2010. Effective removal of Cu (II) ions from aqueous solution by amino-functionalized magnetic nanoparticles. J. Hazard. Mater. 184 (1–3), 392–399.

He, F., Fan, J.T., Ma, D., Zhang, L.M., Leung, C., Chan, H.L., 2010. The attachment of Fe$_3$O$_4$ nanoparticles to graphene oxide by covalent bonding. Carbon 48, 3139–3144.

Ho, Y.S., McKay, G., 1998. Sorption of dye from aqueous solution by peat. Chem. Eng. J. 70 (2), 115–124.

Ho, Y.S., McKay, G., 1999. Pseudo-second order model for sorption processes. Process Biochem. 34 (5), 451–465.

Konstantinou, I.K., Albanis, T.A., 2004. TiO$_2$-assisted photocatalytic degradation of azo dyes in aqueous solution: kinetic and mechanistic investigations – a review. Appl. Catal. B – Environ. 49 (1), 1–14.

Kornaros, M., Lyberatos, G., 2006. Biological treatment of wastewaters from a dye manufacturing company using a trickling filter. J. Hazard. Mater. 136 (1), 95–102.

Lee, J.W., Choi, S.P., Thiruvenkatachari, R., Shim, W.G., Moon, H., 2006. Submerged microfiltration membrane coupled with alum coagulation/powdered activated carbon adsorption for complete decolorization of reactive dyes. Water Res. 3, 435–444.

Li, Y.H., Sun, J.K., Du, Q.J., Zhang, L.H., Yang, X.X., Wu, S.L., Xia, Y.Z., Wang, Z.H., Xia, L.H., Cao, A.Y., 2014. Mechanical and dye adsorption properties of graphene oxide/chitosan composite fibers prepared by wet spinning. Carbohydr. Polym. 102, 755–761.

Liu, C.H., Wu, J.S., Chiu, H.C., Suen, S.Y., Chu, K.H., 2007. Removal of anionic reactive dyes from water using anion exchange membranes as adsorbers. Water Res. 41 (7), 1491–1500.

Liu, F., Chung, S., Oh, G., Seo, T.S., 2012. Three-dimensional graphene oxide nanostructure for fast and efficient water-soluble dye removal. ACS Appl. Mater. Inter. 4 (2), 922–927.

Luo, X., Zhang, L., 2009. High effective adsorption of organic dyes on magnetic cellulose beads entrapping activated carbon. J. Hazard. Mater. 171 (1–3), 340–347.

Madadrang, C.J., Kim, H.Y., Gao, G., Wang, N., Zhu, J., Feng, H., Gorring, M., Kasner, M.L., Hou, S., 2012. Adsorption behavior of EDTA-graphene oxide for Pb (II) removal. ACS Appl. Mater. Inter. 4 (3), 1186–1193.

Meral, K., Metin, O., 2014. Graphene oxide-magnetite nanocomposite as an efficient and magnetically separable adsorbent for methylene blue removal from aqueous solution. Turk. J. Chem. 38, 775–782.

Mittal, A., Mittal, J., Malviya, A., Gupta, V.K., 2010. Removal and recovery of Chrysoidine Y from aqueous solutions by waste materials. J. Colloid Interface Sci. 344 (2), 497–507.

Nurchi, V.M., Crespo-Alonso, M., Biesuz, R., Alberti, G., Pilo, M.I., Spano, N., Sanna, G., 2014. Sorption of chrysoidine by row cork and cork entrapped in calcium alginate beads. Arab. J. Chem. 7 (1), 133–138.

Rhymes, M.R., Smart, K.A., 2001. Effect of storage conditions on the flocculation and cell wall characteristics of an ale brewing yeast strain. J. Am. Soc. Brew. Chem. 59 (1), 32–38.

Saleh, T.A., 2011. The influence of treatment temperature on the acidity of MWCNT oxidized by HNO$_3$ or a mixture of HNO$_3$/H$_2$SO$_4$. Appl. Surf. Sci. 257 (17), 7746–7751.

Saleh, T.A., Agarwal, S., Gupta, V.K., 2011. Synthesis of MWCNT/MnO$_2$ and their application for simultaneous oxidation of arsenite and sorption of arsenate. Appl. Catal. B – Environ. 106 (1–2), 46–53.

Service, R.F., 2009. Materials science carbon sheets an atom thick give rise to graphene dreams. Science 324 (5929), 875–877.

Shi, H.C., Li, W.S., Zhong, L., Xu, C.J., 2014. Methylene blue adsorption from aqueous solution by magnetic cellulose/graphene oxide composite: equilibrium, kinetics, and thermodynamics. Ind. Eng. Chem. Res. 53, 1108–1118.

Vadivelan, V., Kumar, K.V., 2005. Equilibrium, kinetics, mechanism, and process design for the sorption of methylene blue onto rice husk. J. Colloid Interface Sci. 286 (1), 90–100.

Wang, C., Feng, C., Gao, Y.J., Ma, X.X., Wu, Q.H., Wang, Z., 2011. Preparation of a graphene-based magnetic nanocomposite for the removal of an organic dye from aqueous solution. Chem. Eng. J. 173, 92–97.

Wang, J., Zheng, S., Shao, Y., Liu, J., Xu, Z., Zhu, D., 2010. Amino-functionalized $Fe_3O_4@SiO_2$ core-shell magnetic nanomaterial as a novel adsorbent for aqueous heavy metals removal. J. Colloid Interface Sci. 349 (1), 293–299.

Wu, X.L., Wang, L., Chen, C.L., Xu, A.W., Wang, X.K., 2011. Water-dispersible magnetite-graphene-LDH composites for efficient arsenate removal. J. Mater. Chem. 21 (43), 17353–17359.

Wu, Z.S., Ren, W., Wen, L., Gao, L., Zhao, J., Chen, Z., Zhou, G., Li, F., Cheng, H.M., 2010. Graphene anchored with Co_3O_4 nanoparticles as anode of lithium ion batteries with enhanced reversible capacity and cyclic performance. ACS Nano 4 (6), 3187–3194.

Xie, G.Q., Xi, P.X., Liu, H.Y., Chen, F.J., Huang, L., Shi, Y.J., Hou, F.P., Zeng, Z.Z., Shao, C.W., Wang, J., 2012. A facile chemical method to produce superparamagnetic graphene oxide–Fe_3O_4 hybrid composite and its application in the removal of dyes from aqueous solution. J. Mater. Chem. 22, 1033–1039.

Yang, X.Y., Zhang, X.Y., Ma, Y.F., Huang, Y., Wang, Y.S., Chen, Y.S., 2009. Superparamagnetic graphene oxide–Fe_3O_4 nanoparticles hybrid for controlled targeted drug carriers. J. Mater. Chem 19, 2710–2714.

Yan, K., Qiu, Y., Chen, W., Zhang, M., Yang, S., 2011. A double layered photoanode made of highly crystalline TiO_2 nanooctahedra and agglutinated mesoporous TiO_2 microspheres for high efficiency dye sensitized solar cells. Energy Environ. Sci. 4 (6), 2168–2176.

Zhou, C.J., Zhang, W.J., Wang, H.X., Li, H.Y., Zhou, J., Wang, S.H., Liu, J.Y., Luo, J., Zou, B.S., Zhou, J.D., 2014. Preparation of Fe_3O_4-embedded graphene oxide for removal of methylene blue. Arab. J. Sci. Eng. 39, 6679–6685.